Cryo-EM structures of *Escherichia coli* cytochrome bo_3 reveal bound phospholipids and ubiquinone-8 in a dynamic substrate binding site

Jiao Li[a,b,1], Long Han[b,1], Francesca Vallese[c,d,1], Ziqiao Ding[e], Sylvia K. Choi[e], Sangjin Hong[e], Yanmei Luo[a], Bin Liu[a], Chun Kit Chan[f], Emad Tajkhorshid[e], Jiapeng Zhu[a,2], Oliver Clarke[c,d,2], Kai Zhang[b,2], and Robert Gennis[e,2]

[a]School of Medicine and Holistic Integrative Medicine, Nanjing University of Chinese Medicine, Nanjing 210023, China; [b]Department of Molecular Biophysics and Biochemistry, Yale University, New Haven, CT 06511; [c]Department of Anesthesiology, Columbia University, New York, NY 10032; [d]Department of Physiology and Cellular Biophysics, Columbia University, New York, NY 10032; [e]Department of Biochemistry, University of Illinois at Urbana–Champaign, Urbana, IL 61801; and [f]Department of Physics, University of Illinois at Urbana–Champaign, Urbana, IL 61801

Edited by Harry B. Gray, California Institute of Technology, Pasadena, CA, and approved July 14, 2021 (received for review April 11, 2021)

Two independent structures of the proton-pumping, respiratory cytochrome bo_3 ubiquinol oxidase (cyt bo_3) have been determined by cryogenic electron microscopy (cryo-EM) in styrene–maleic acid (SMA) copolymer nanodiscs and in membrane scaffold protein (MSP) nanodiscs to 2.55- and 2.19-Å resolution, respectively. The structures include the metal redox centers (heme *b*, heme o_3, and Cu_B), the redox-active cross-linked histidine–tyrosine cofactor, and the internal water molecules in the proton-conducting D channel. Each structure also contains one equivalent of ubiquinone-8 (UQ8) in the substrate binding site as well as several phospholipid molecules. The isoprene side chain of UQ8 is clamped within a hydrophobic groove in subunit I by transmembrane helix TM0, which is only present in quinol oxidases and not in the closely related cytochrome *c* oxidases. Both structures show carbonyl O1 of the UQ8 headgroup hydrogen bonded to D75^{I} and R71^{I}. In both structures, residue H98^{I} occupies two conformations. In conformation 1, H98^{I} forms a hydrogen bond with carbonyl O4 of the UQ8 headgroup, but in conformation 2, the imidazole side chain of H98^{I} has flipped to form a hydrogen bond with E14^{I} at the N-terminal end of TM0. We propose that H98^{I} dynamics facilitate proton transfer from ubiquinol to the periplasmic aqueous phase during oxidation of the substrate. Computational studies show that TM0 creates a channel, allowing access of water to the ubiquinol headgroup and to H98^{I}.

ubiquinone | heme–copper oxidoreductase | electron transport | bioenergetics | proton pump

The proton-pumping heme–copper oxygen reductases serve as the terminal enzymes in the aerobic respiratory chains of most aerobic organisms and catalyze the four-electron reduction of O_2 to water coupled to the generation of a proton motive force. These transmembrane O_2 reductases are members of the superfamily of heme–copper oxidoreductases (HCOs)[1] that also includes nitric oxide reductases. There are three families of respiratory heme–copper O_2 reductases (A, B, and C) with the A-family, which includes the mitochondrial cyt *c* oxidases, being the largest and most extensively studied. Most of the A-family HCOs use a ferrous cyt *c* (cyt c_{red}) as a one-electron donor, with four sequential one-electron reactions required to reduce O_2 to 2 H_2O.

$$4\,\text{cyt}\;c_{red} + O_2 + 8\,H^{+}_{in} \rightleftarrows 4\,\text{cyt}\;c_{ox} + 2\,H_2O + 4\,H^{+}_{out}.$$

Each electron delivered to the active site of the enzyme by the oxidation of cyt c_{red} at a site on the outer (electrically positive) side of the membrane results in the uptake of two protons from the inside (electrically negative) surface of the membrane. One proton (per electron) is consumed in generating H_2O, whereas the second proton is pumped electrogenically across the membrane.

A subfamily of A-family HCOs uses membrane-bound quinols as the source of electrons in place of cyt c_{red} (1). The quinol oxidases lack the docking site for cyt c_{red} as well as the Cu_A redox center that is the initial site of entry of electrons in the cyt *c* oxidases. In their place, the quinol oxidases have acquired a quinol binding site exposed to the hydrophobic lipid bilayer which catalyzes the two-electron oxidation of the quinol substrate, usually either ubiquinol or menaquinol, near the outer surface of the membrane. The natural substrate for *Escherichia coli* cyt bo_3 is ubiquinol-8. The oxidation of each quinol, therefore, releases two protons on the outer, electrically positive side of the membrane (2–5).

$$2\,QH_2 + O_2 + 8\,H^{+}_{in} \rightleftarrows 2\,Q + 2\,H_2O + 8\,H^{+}_{out}.$$

As first reported by the Wikström group, the quinol oxidases also generate a proton motive force and pump protons across the membrane in the same way as do the cyt *c* oxidases (6–8). Importantly, the quinol binding site stabilizes the one-electron–reduced semiquinone state of the quinone, facilitating the oxidation of the quinol in two one-electron steps. A major question has been to

Significance

Quinol oxidases that are members of the heme–copper superfamily of respiratory oxygen reductases have evolved from cytochrome *c* oxidases. They directly oxidize quinol and reduce oxygen to water. Here, we describe two high-resolution cryogenic electron microscopy structures of the proton-pumping cytochrome bo_3 ubiquinol oxidase in styrene–maleic acid copolymer nanodiscs and in membrane scaffold protein nanodiscs. Each structure contains one equivalent of well-resolved ubiquinone-8 in the substrate binding site as well as several phospholipid molecules. These structures indicate that H98^{I} has two conformations that allow H98^{I} hydrogen bonded to carbonyl O4 of the UQ8 or with E14^{I}. We propose that H98^{I} dynamics serves to shuttle protons from ubiquinol-8 via E14^{I} to the bulk aqueous phase upon ubiquinol-8 oxidation.

Author contributions: J.L., J.Z., O.C., K.Z., and R.G. designed research; J.L., L.H., F.V., Y.L., C.K.C., E.T., and K.Z. performed research; Z.D., S.K.C., S.H., Y.L., J.Z., O.C., and R.G. analyzed data; and J.L., F.V., Z.D., S.K.C., B.L., C.K.C., E.T., J.Z., O.C., K.Z., and R.G. wrote the paper.

The authors declare no competing interest.

This article is a PNAS Direct Submission.

[1]J.L., L.H., and F.V. contributed equally to this work.

[2]To whom correspondence may be addressed. Email: r-gennis@illinois.edu, jack.zhang@yale.edu, oc2188@cumc.columbia.edu, or zhujiapeng@hotmail.com.

This article contains supporting information online at https://www.pnas.org/lookup/suppl/doi:10.1073/pnas.2106750118/-/DCSupplemental.

define the quinone binding site(s) that evolved to convert the cyt *c* oxidase into a ubiquinol oxidase. There are several amino acid residues that are conserved only in quinol oxidases as well as an additional transmembrane helix in subunit I (TM0) that is only present in quinol oxidases but not in the closely related cyt *c* oxidases. Although many studies have been interpreted to indicate that there are two ubiquinol binding sites, high affinity and low affinity (9), recent data strongly suggests that there is only a single binding site for ubiquinol in cyt bo_3 (10, 11).

The structure of cyt bo_3 in 1% n-octyl-β-D-glucopyranoside detergent was obtained by X-ray crystallography over 20 years ago by Abramson et al. (12). Due to the presence of this harsh detergent, phospholipids and ubiquinone are absent, and the structure lacks about 25% of the total amino acid residues, including TM0 in subunit I. Resolution was limited to 3.5 Å at best. Nevertheless, the structure did reveal that several amino acid residues that are conserved in ubiquinol oxidases were reasonable candidates for interacting with the headgroup of the ubiquinol substrate. This work was accompanied by extensive mutagenesis studies.

Mutagenesis studies have confirmed the functional importance of R71^{I} (superscript indicates subunit I), D75^{I}, and H98^{I} (12, 13). Subsequent spectroscopic techniques, particularly pulsed EPR (electron paramagnetic resonance) analysis of the ubisemiquinone radical stabilized at the binding site, have confirmed that these three residues interact with the UQ8 in addition to a fourth residue, Q101^{I}, that interacts very weakly with the protein-bound ubisemiquinone (10, 14–18). The pulsed EPR studies suggested that carbonyl O1 of the ubisemiquinone is hydrogen bonded by both the carboxyl group of D75^{I} and N_{ε} of R71^{I}, whereas carbonyl O4 is hydrogen bonded to H98^{I}. Based on a Q-band ENDOR (electron nuclear double resonance) study (14), the two hydrogen bonds to carbonyl O1 were predicted to be out of the plane of the ubiquinone ring and on opposite sides. This study also indicated that the hydrogen bond between D75^{I} and carbonyl O1 is far from optimal geometry, being perpendicular to the ring of the quinone headgroup.

Recently, we reported (19) the crystal structure of the cyt aa_3-600 menaquinol oxidase from *Bacillus subtilis*, a close homolog of *E. coli* cyt bo_3. The X-ray structure was determined using protein in the presence of the relatively mild detergent n-dodecyl-β-D-maltoside (DDM). The structure of cyt aa_3-600 has similar resolution as the previously reported structure of cyt bo_3, but the equivalent portions of the protein missing in the cyt bo_3 structure are present. In addition, menaquinone-7 is present but poorly resolved. Of particular importance, subunit I TM0, unique to quinol oxidases, is shown to form part of the quinone binding site.

While preparing this manuscript, a cryogenic electron microscopy (cryo-EM) methods publication demonstrated that the cyt bo_3 structure could be codetermined together with other proteins in the *E. coli* membrane using the "build and retrieve" approach (20). The structure confirmed the previous biochemical prediction of the single UQ8 binding site (10, 14). However, due to the poor density in the region of the UQ8 binding site, details of how UQ8 interacts with its surrounding are not clear. The resolution of the UQ8 binding site of the current two structures provide detailed structural information of the protein in two different states and, furthermore, resolve a number of internal water molecules within the protein as well as detailed protein–lipid interactions.

One structure (2.55-Å resolution) in the current work was determined using protein embedded in styrene–maleic acid copolymer (SMA) nanodiscs (21–25). The protein was extracted from native *E. coli* membranes and purified in SMA rather than traditional detergents. The second structure (2.19-Å resolution) reported here was determined using protein extracted from native *E. coli* membranes using the detergent DDM and then reconstituted with membrane scaffold protein (MSP) nanodiscs (26–28) in a bilayer of POPG (1-palmitoyl-2-oleoyl-sn-glycero-3-(phospho-rac-(1-glycerol))). The structure of cyt bo_3 in MSP nanodiscs was determined in the presence of Zn^{2+} and reveals a zinc binding site composed of four methionine residues contributed by three different subunits. The third structure (2.20-Å resolution) reported by Su et al. (20) was also determined using protein extracted from *E. coli* membranes using the detergent DDM and reconstituted in MSP nanodiscs using extracted *E. coli* lipids.

Both of the structures reported in the current work contain all the expected features of an A-family HCO (i.e., a water-filled, proton-conducting D channel, K channel, a low-spin heme, and the heme–copper binuclear center. In each structure, the headgroup of the bound UQ8 is tucked in a pocket in subunit I between TM0, TM1, TM2, and TM3, with the hydrophobic tail clamped by TM0 to a hydrophobic groove formed by TM1 and TM3, making clear the functional importance of this additional transmembrane helix (TM0), which is only present in the quinol oxidases. Computational studies confirm that the presence of TM0 hinders dissociation of the quinone from the protein but also shows conformational flexibility of TM0 that might facilitate dissociation of the oxidized product on a longer msec timeframe consistent with catalytic turnover. The two structures show that H98^{I} can form a hydrogen bond to carbonyl O4 of UQ8 in one conformation and a hydrogen bond with E14^{I} when its side chain is flipped away. It is suggested that H98^{I} dynamics serve to shuttle protons from ubiquinol-8 via E14^{I} to the bulk aqueous phase upon oxidation of the substrate. Computational studies reveal that the presence of TM0 creates an aqueous channel allowing hydration of the region around the ubiquinol headgroup. Water molecules are essential to allow proton diffusion from the quinol headgroup to the bulk aqueous phase.

Results

A Layer of Structured Lipids Is Observed in the SMA-Purified cyt bo_3.

Cyt bo_3 was isolated using SMA, which extracts the protein in a patch of native cell membrane. A set of 209,984 particles were used to rebuild a map at 2.64-Å resolution that best resolved a thin layer of lipids around the protein. The lipids adjacent to the protein are highly structured, as indicated by the well-defined density of lipid acyl tails. The acyl tails are not strictly perpendicular to the membrane interface but follow the protein contour to interact with the hydrophobic sidechains of the protein (Fig. 1 *A* and *B*). A layer of lipids was also resolved in the cyt bo_3 solubilized using the detergent DDM and reconstituted into MSP nanodiscs, and the layer is almost identical to that of the SMA-purified protein. In each protein preparation, all four subunits of the enzyme are resolved and are essentially in the same conformation (Fig. 1 *C* and *D*).

Protein-Bound Phospholipids Observed in Both SMA-Purified and MSP Nanodisc-Reconstituted cyt bo_3.

Both enzyme preparations revealed well-resolved individual phospholipid molecules. Five PE (phosphatidylethanolamine) molecules are well resolved and modeled in the SMA-purified cyt bo_3. Two PE molecules are in the groove formed by TM0, TM1, and TM2 on the cytoplasmic side of the protein below the binding site for UQ8. Three PE molecules are buried in the crevice between subunit I and III, near TM13 and TM14. These are shown in Fig. 2*A*.

In the MSP nanodisc–reconstituted cyt bo_3, 12 phospholipid molecules were resolved including 5 in approximately the same locations as those resolved in the SMA-purified preparation of the protein (Fig. 2*B*). The nanodiscs were reconstituted with POPG, and all the phospholipids were modeled as phosphatidylglycerols in cases where the headgroup could not be unambiguously identified. Two PE molecules and a cardiolipin molecule, presumably carried through from native *E. coli* lipids, are also observed.

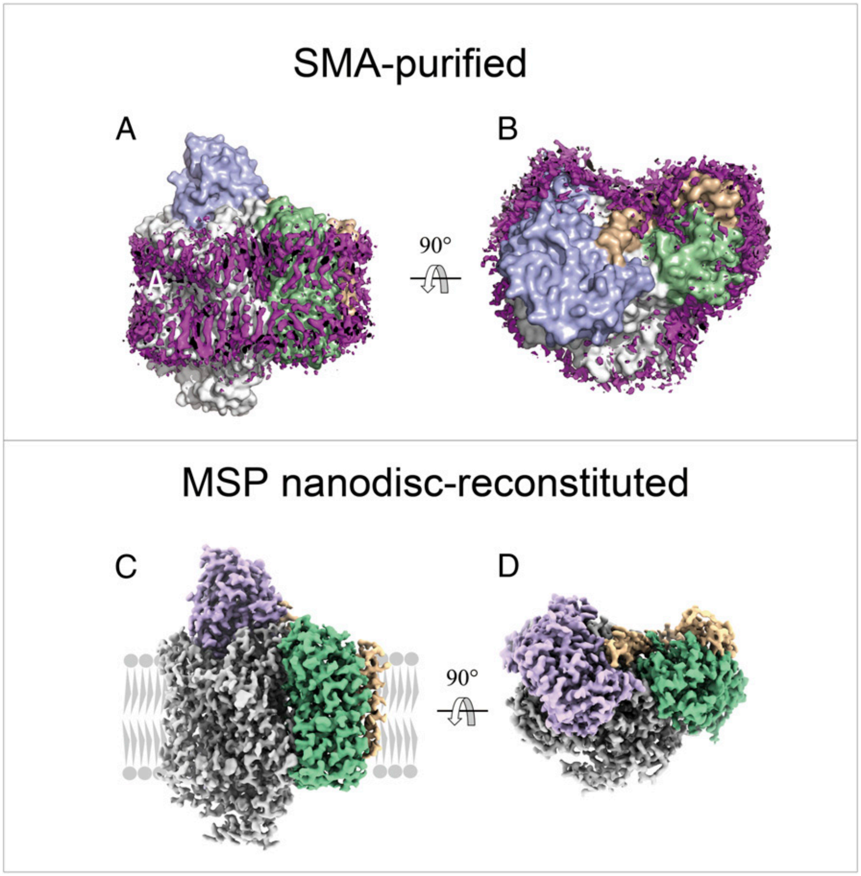

Fig. 1. Overall structure of cyt bo_3. Side view (*A*) and top view (*B*) of SMA-purified cyt bo_3 surrounded by a layer of native membrane lipids. The four subunits are color-coded: subunit I (white), II (blue), III (green), and IV (wheat). Purple EM densities represent the structured lipids bound to the protein. Side view (*C*) and top view (*D*) of cryo-EM structure of cyt bo_3 in MSP nanodiscs. The four subunits are color coded: subunit I (white), II (purple), III (green), and IV (wheat). In panel (*C*), the membrane is represented in gray.

Two Conformations of H98$^{\text{I}}$. Residue H98$^{\text{I}}$ exhibits two conformations in the structure of the SMA-purified cyt bo_3 (Fig. 3*C*). In conformation 1, H98$^{\text{I}}$ is hydrogen bonded to carbonyl O4 of UQ8 (N$_{\varepsilon}$, 2.4 Å; Table 1), whereas in conformation 2, the imidazole sidechain has flipped and forms a hydrogen bond with the carboxyl of E14$^{\text{I}}$ (N$_{\varepsilon}$, 3.1 Å; Table 1).

The structure of the MSP nanodisc–reconstituted cyt bo_3 is similar to the SMA-purified cyt bo_3: in conformaion 1, H98$^{\text{I}}$ is hydrogen bonded to carbonyl O4 of UQ8 (N$_{\varepsilon}$, 2.3 Å; Table 1), whereas in conformation 2, the imidazole sidechain has flipped and is 4.0 Å from the carboxyl of E14$^{\text{I}}$ (Table 1 and Fig. 3*C*).

Both Structures Contain a Single Molecule of UQ8.

The hydrophobic quinone tail and TM0. Both the cryo-EM structures reveal a groove formed by TM0, TM1, and TM2 that contains one molecule of UQ8 at the periplasmic side and two phospholipids bound at the cytoplasmic side (Fig. 3*A*). In the SMA-purified preparation of the enzyme, only five of the eight isoprene units in the hydrophobic tail are resolved. In the MSP nanodisc–reconstituted cyt bo_3, the entire quinone tail is resolved. The first five isoprene units of UQ8 in the MSP nanodisc–reconstituted enzyme roughly overlap with those observed in the SMA-purified enzyme preparation (Fig. 3*C*). Whereas the first several isoprene units after the headgroup are directed perpendicular to the plane of the membrane, the tail turns and runs parallel to the plane of the membrane as it wraps around TM0 and finally turns back toward the periplasmic surface. TM0 largely buries most of UQ8 (Fig. 3*B*). The hydrophobic tail of the UQ8 wraps around and is clamped to the protein by TM0. The last portion of the UQ8 tail sticks out of the protein and protrudes into the membrane bilayer. Although two ordered PE lipids are bound at the cytoplasmic side of the protein just below the UQ8, there is no direct contact between the bound UQ8 and bound PE on the enzyme surface.

Both structures suggest that the binding of the substrate, ubiquinol-8, and dissociation of the oxidized product, UQ8, would be facilitated by movement of TM0 to release the apparent clamp. Indeed, there is little direct interaction between TM0 and the rest of the protein that would serve to keep TM0 in place. The key interaction appears to be a likely hydrogen bond formed between E14$^{\text{I}}$ and His98$^{\text{I}}$ that is observed in both the MSP nanodisc–reconstituted and SMA-purified proteins (Fig. 3*C*).

The quinone headgroup. The quinone headgroup is located ∼14 Å (center to center) from heme *b*, the electron acceptor for the two one-electron oxidation steps to fully oxidize ubiquinol-8. Fig. 4*A* shows the relative positions in the SMA-purified cyt bo_3 of the bound UQ8, heme *b*, and four residues that are known to interact with the headgroup of the one-electron–reduced semiquinone state, R71$^{\text{I}}$, D75$^{\text{I}}$, H98$^{\text{I}}$, and Q101$^{\text{I}}$. Comparing the two structures of cyt bo_3, there are small but significant differences in the position of the UQ8 headgroup and its hydrogen bonding interactions with nearby residues (Table 1). Fig. 4 *B* and *C* show the position of the quinone headgroup for the SMA-purified and MSP nanodisc–reconstituted preparations of cyt bo_3. In conformation 1 of the SMA-purified enzyme, UQ8 carbonyl O1 is near both D75$^{\text{I}}$ (3.5 Å) and R71$^{\text{I}}$ (N$_{\eta}$, 2.7 Å and N$_{\varepsilon}$, 3.1 Å), whereas H98$^{\text{I}}$ (N$_{\varepsilon}$)

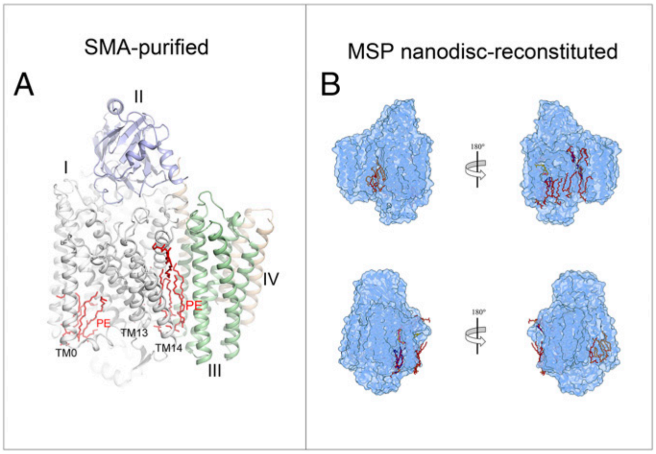

Fig. 2. Each structure contains one equivalent of well-resolved UQ8 in the substrate binding site as well as several phospholipid molecules. (*A*) Five tightly bound PE molecules (red) that "glue" TM0, TM13, and TM14 to the enzyme. (*B*) Comparison of lipids between those in the cyt *bo*$_3$ EM structure in MSP nanodisc (in red POPG, in brown PE, and in orange CDL) and those in the structure in SMA-purified cyt *bo*$_3$ (in blue PE). UQ8 is depicted in yellow for cyt *bo*$_3$ reconstituted in MSP nanodisc and in magenta for SMA-purified cyt *bo*$_3$.

is 2.4 Å from O4 of the UQ8. The sidechain nitrogen of Q101$^{\text{I}}$ is 6.5 Å from O4 of UQ8, too distant to form a hydrogen bond. In addition, E14$^{\text{I}}$ is 4.4 Å from H98$^{\text{I}}$ (N_ε) of conformation 1.

In the structure of the MSP nanodisc–reconstituted enzyme, UQ8 carbonyl O1 is clearly hydrogen bonded to both D75$^{\text{I}}$ (3.4 Å) and R71$^{\text{I}}$ (N_η, 2.7 Å and N_ε, 3.0 Å), while carbonyl O4 is hydrogen bonded to H98$^{\text{I}}$ (N_ε, 2.3 Å) in conformation 1. However, as shown in Figs. 3*C* and 4*C* and Table 1, in conformation 2 of both enzymes, the orientation of the imidazole sidechain of H98$^{\text{I}}$ precludes a hydrogen bond to O4 of UQ8 (7.7 Å in MSP nanodisc–reconstituted protein and 7.3 Å in SMA-purified protein, respectively, from the imidazole N_ε). In conformation 2, a hydrogen bond is plausible between the sidechain of E14$^{\text{I}}$ and N_ε of H98$^{\text{I}}$ (4.0 Å in MSP nanodisc–reconstituted protein and 3.1 Å in SMA-purified protein). The sidechain Q101$^{\text{I}}$ is far from O4 of UQ8 (7.2 Å in MSP nanodisc–reconstituted protein and 6.5 Å in SMA-purified protein) in both structures.

Suggested Dynamics of the Transmembrane Helices at the UQ8 Binding Site. In addition to the different conformational states of H98$^{\text{I}}$, there are some data suggesting larger conformational flexibility of the helices comprising the UQ8 binding site. Four maps rebuilt with four different three-dimensional (3D) classes revealed significant conformational changes around the UQ8 binding site. The map rebuilt with the majority of the particles (57%) has well-defined density of the bound UQ8 (*SI Appendix*, Fig. S6*A*) along with the nearby lipids and amino acid residues. The other three maps display different degrees of low-density region around the UQ8 binding site (*SI Appendix*, Fig. S6 *B*–*D*). Together, low density in the alternate maps of the region of the protein at the UQ8 binding site suggests that this region of the protein has multiple conformations and may indicate dynamics of the protein required to facilitate rapid binding and dissociation of the quinone substrate/product at this site.

Histidine–Tyrosine Cross-Link and Internal Water Molecules. Both cyt *bo*$_3$ structures have structural features that are found in structures of other A-family heme–copper oxygen reductases. All heme–copper oxygen reductases contain a unique cross-linked histidine–tyrosine cofactor at the active site. This is also observed in all the cryo-EM structures of cyt *bo*$_3$. *SI Appendix*, Fig. S7*A* shows the cross-link between H284$^{\text{I}}$ and Y288$^{\text{I}}$ in the structure of the SMA-purified cyt *bo*$_3$ superimposed on the structure of from the $\alpha\alpha_3$-type cyt *c* oxidase from *Rhodobacter sphaeroides*.

The A-family heme–copper oxygen reductases all contain a proton-conducting D channel that contains a string of structurally resolved internal water molecules that act as a proton wire connecting the entrance of the D channel, D135$^{\text{I}}$ in cyt *bo*$_3$ to the branchpoint (E286$^{\text{I}}$ in cyt *bo*$_3$). Beyond E286$^{\text{I}}$, protons taken up by the D channel are directed either to the active site (chemical protons) or to the proton loading site (pumped protons). The cryo-EM structure from both enzyme preparations contains numerous structurally resolved water molecules that include those that help form the proton wire in the D channel. As in previous structures of A-family heme–copper oxygen reductases, there is a gap in the chain of water molecules at the so-called "neck" of the D channel between N142$^{\text{I}}$ and N124$^{\text{I}}$. The water chain within the D channel from the MSP nanodisc–reconstituted preparation is shown in *SI Appendix*, Fig. S7*B*.

A New Zn^{2+} Binding Site Is Shared by Subunits I, II, and IV. The structure of the MSP nanodisc–reconstituted cyt *bo*$_3$ was determined in the presence of Zn^{2+}. This has revealed a Zn^{2+} binding site at the periplasmic surface of the protein that is not observed in the SMA-solubilized enzyme. *SI Appendix*, Fig. S8*A* shows the Zn^{2+} bound to four methionines—two from subunit II and one each from subunit I and subunit IV. Although no Zn^{2+} is present in the structure of the SMA-solubilized protein, the four methionines are present in the same location. *SI Appendix*, Fig. S8*B* is a superposition of the structure of the SMA-purified enzyme

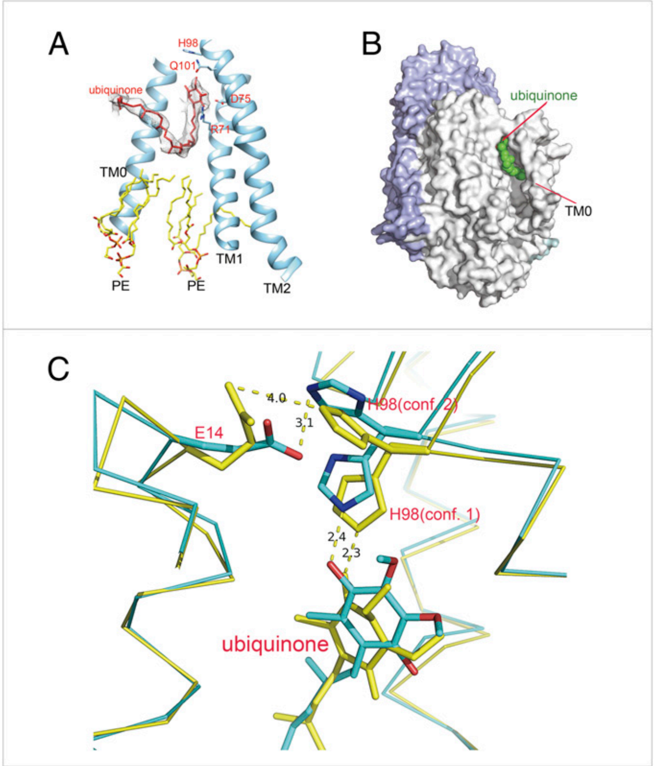

Fig. 3. Ubiquinone binding site. (*A*) A UQ8 in cyt *bo*$_3$ EM structure in MSP nanodisc is bound in the groove formed by TM0, TM1, and TM2. The head group of the ubiquinone is hydrogen bonded with residues R71$^{\text{I}}$ and D75$^{\text{I}}$. (*B*) Surface representation of a UQ8 molecule bound in the groove formed by TM0, TM1, and TM2. (*C*) Superposition of the cyt *bo*$_3$ EM structure in MSP nanodiscs (yellow) and in SMA (green). In both cyt *bo*$_3$ structures, the density of H98$^{\text{I}}$ indicates dual conformations, and "conformation 2" of H98$^{\text{I}}$ is likely to form hydrogen bond with E14$^{\text{I}}$.

Table 1. Distances between key residues and between these residues and UQ8

		SMA-purified enzyme (conf. 1)	SMA-purified enzyme (conf. 2)	MSP nanodisc– reconstituted enzyme (conf. 1)	MSP nanodisc– reconstituted enzyme (conf. 2)
H98$^{\mathrm{I}}$ (N_ε)	E14$^{\mathrm{I}}$	4.4 Å	**3.1 Å**	8.6 Å	4.0 Å
H98$^{\mathrm{I}}$ (N_ε)	UQ8 (O4)	**2.4 Å**	7.3 Å	**2.3 Å**	7.7 Å
R71$^{\mathrm{I}}$ (N_η)	UQ8 (O1)	**2.7 Å**		**2.7 Å**	
R71$^{\mathrm{I}}$ (N_ε)	UQ8 (O1)	**3.1 Å**		**3.0 Å**	
D75$^{\mathrm{I}}$	UQ8 (O1)	**3.5 Å**		**3.4 Å**	
Q101$^{\mathrm{I}}$	UQ8 (O4)	6.5 Å		7.2 Å	

Bold font indicates possible hydrogen bond.

on the Zn^{2+} binding site from the MSP nanodisc–reconstituted cyt bo_3.

Computational Studies Indicate That TM0 Facilitates Hydration to Protonatable Residues That Interact with UQ8. TM0, TM1, and TM2 form a groove in which UQ8 binds to cyt bo_3 (Fig. 3*A*) and can hydrogen bond to residues R71$^{\mathrm{I}}$, D75$^{\mathrm{I}}$, and H98$^{\mathrm{I}}$ (Fig. 4 *B* and *C*). Likely functional roles for these residues are to facilitate the deprotonation of the ubiquinol-8 that must accompany its oxidation and to stabilize the ubisemiquinone intermediate as well as to participate in the transfer of these protons to the bulk solution surrounding the protein. The access of this region to water from the bulk solution was explored using computational methods.

Molecular dynamics (MD) simulations of cyt bo_3 and its mutant ΔTM0, where TM0 is removed, show that the mean number of water molecules found along the groove, from H98$^{\mathrm{I}}$ to R71$^{\mathrm{I}}$, is consistently higher for the wild-type enzyme than for the mutant ΔTM0 in which TM0 has been removed (Fig. 5*A*). Our simulation results match the measurement using Caver (29), which shows that the size of the groove from H98$^{\mathrm{I}}$ to R71$^{\mathrm{I}}$ is larger in the wild-type cyt bo_3 than in ΔTM0 (Fig. 5*C*). The groove in the vicinity of H98$^{\mathrm{I}}$ serves as an entrance for water molecules from the bulk solution. In the wild type, the radius for the groove near H98$^{\mathrm{I}}$ is around 0.65 Å, which is much larger than 0.07 Å found for the ΔTM0 mutant. One reason for this is that, in the absence of TM0, phospholipid molecules from the surrounding bilayer invade this region and greatly reduce the hydration in the vicinity of the quinol headgroup. Thus, the MD simulations and Caver measurements both suggest that the presence of TM0 enhances the hydration of the groove, particularly around H98$^{\mathrm{I}}$ and the headgroup of the ubiquinol. This enhanced hydration is likely to facilitate the essential proton transfer from the ubiquinol-8 headgroup to the bulk solution that accompanies oxidation of the quinol.

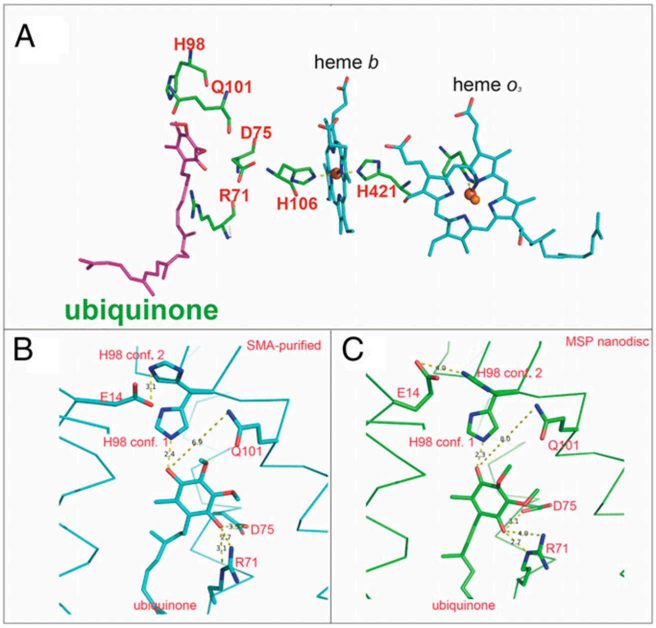

Fig. 4. UQ8 and key residues. (*A*) The UQ8 resides close to R71$^{\mathrm{I}}$, D75$^{\mathrm{I}}$, H98$^{\mathrm{I}}$, and Q101$^{\mathrm{I}}$. The distance between the UQ8 headgroup and heme *b* is ∼14 Å (center to center). (*B*) In the SMA-purified enzyme, H98$^{\mathrm{I}}$ has two conformations. The UQ8 is hydrogen bonded with R71$^{\mathrm{I}}$, D75$^{\mathrm{I}}$, and H98$^{\mathrm{I}}$ ("conformation 1", Nε). Q101$^{\mathrm{I}}$ is 6.5 Å from O4 of UQ8. H98$^{\mathrm{I}}$ ("conformation 2", Nε) is hydrogen bonded with E14$^{\mathrm{I}}$. (*C*) In the MSP nanodisc structure, the UQ8 is hydrogen bonded with R71$^{\mathrm{I}}$, D75$^{\mathrm{I}}$, and H98$^{\mathrm{I}}$ ("conformation 1", Nε). Q101$^{\mathrm{I}}$ is 7.2 Å from O4 of UQ8. H98$^{\mathrm{I}}$ ("conformation 2", Nε) is 4.0 Å from E14$^{\mathrm{I}}$.

Computational Studies Indicate That Removal of TM0 Facilitates UQ8 Exit from cyt *bo₃*. Cyt bo_3 oxidizes ubiquinol-8 and pumps protons across the membrane. For this process to run continuously, oxidized UQ8 needs to be released from cyt bo_3 to the membrane. The UQ8 binding pocket in cyt bo_3 can then be occupied by a reduced ubiquinol-8 for the next round of electron transfer and proton translocation.

MD simulations on the wild-type cyt bo_3 and its mutant, ΔTM0, show that the presence of TM0 impacts UQ8 exit from cyt bo_3. Our simulations show that the separation of UQ8 headgroup from cyt bo_3 in ΔTM0 is, for most of the time, greater than that in the wild type (Fig. 5*D*). Consistent with this observation, in ΔTM0, the distribution of the RMSD of the UQ8 headgroup with respect to its position in the UQ8 binding pocket skews toward values higher than for the wild type (Fig. 5*E*). The mean RMSD measured for ΔTM0 is 6.25 Å, with a SD of 1.86 Å, whereas the mean RMSD measured for the wild type is 3.60 Å, with a SD of 2.03 Å. Thus, the peak of the RMSD distribution for ΔTM0 and that for the wild type, which both resemble a Gaussian distribution, separate from one another for at least 1 SD. Therefore, UQ8 is more mobile in ΔTM0 than in the wild type.

The impact of TM0 on UQ8 exist is also revealed by the UQ8–protein interaction. Our MD simulations show that the time evolution of the number of contacts between UQ8 and cyt bo_3 in ΔTM0 is very different from that in the wild type. In ΔTM0, the number of contacts between UQ8 and cyt bo_3 slowly decreases as UQ8 departs from the protein (*SI Appendix*, Fig. S11*A*). In contrast, the number of contacts between UQ8 and cyt bo_3 increases in the wild type (*SI Appendix*, Fig. S11*A*). A breakdown shows that the number of contacts between UQ8 and cyt bo_3, excluding those made with TM0, stably fluctuates around 20 over the time of our simulation, whereas the number of contacts between UQ8 and TM0 increases over time (*SI Appendix*, Fig. S11*B*). This increase correlates with the slight increase in the separation between the headgroup of UQ8 and cyt bo_3 (Fig. 5*D*) and suggests that UQ8 is physically blocked by TM0 as it attempts to leave the groove region of cyt bo_3.

Molecular visualizations (Fig. 5*F*) of the positions of UQ8 headgroups across MD simulations show that UQ8 slowly separates from wild-type cyt bo_3 and remains trapped in the groove region with its headgroup increasingly pressed toward TM0. In

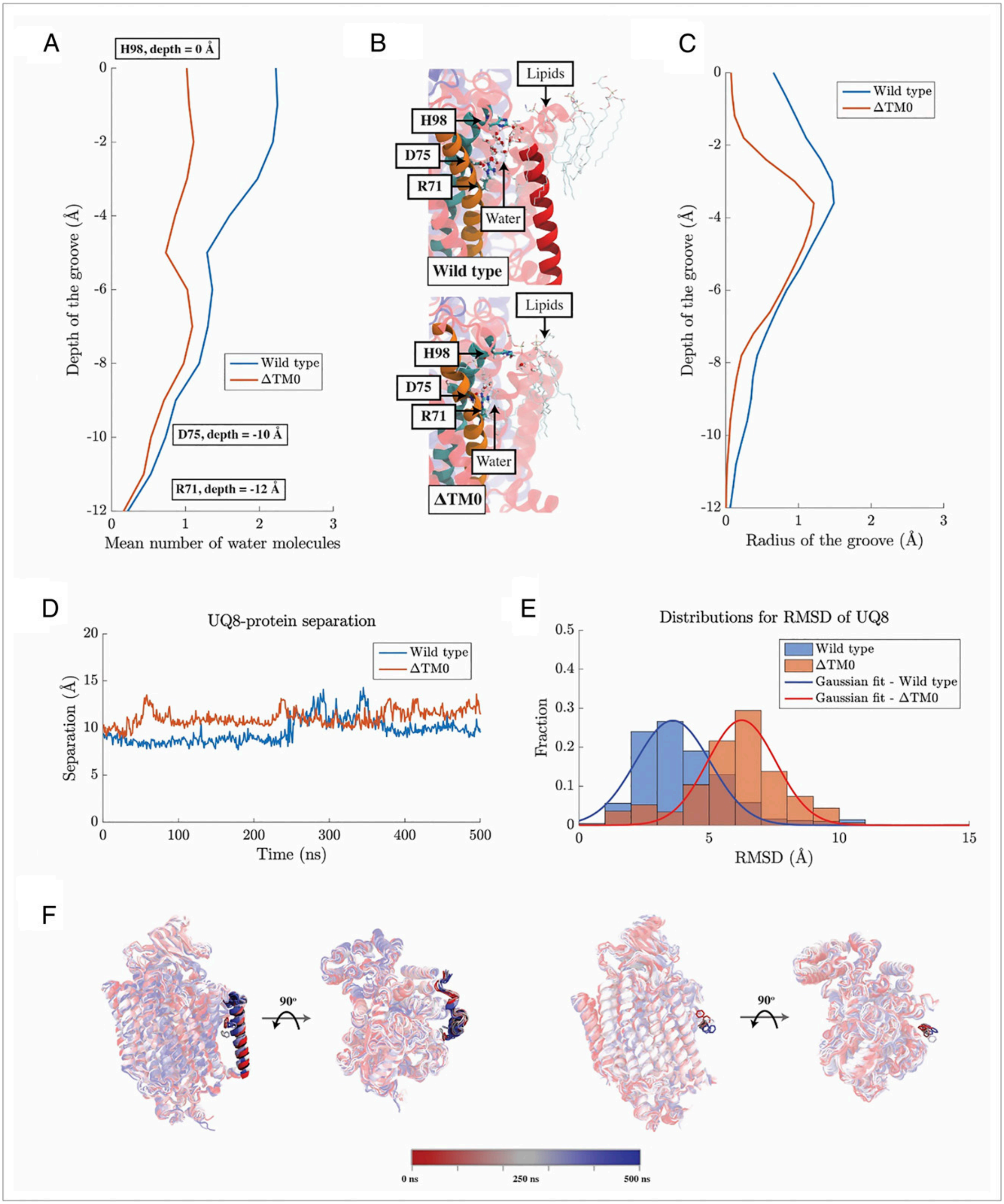

Fig. 5. Impacts of TM0 on the function of cyt bo_3. (*A*) The number of water molecules observed in the groove region of cyt bo_3 and its mutant, ΔTM0, averaged over respective MD trajectories. (*B*) Molecular visualizations of water molecules in the groove region of cyt bo_3 and its mutant. The groove region for the wild-type cyt bo_3 is defined as the space formed among TM0 (solid red), TM1 (solid orange), and TM2 (solid cyan). For ΔTM0, this region corresponds to the water permeable space right outside TM1 and TM2. (*C*) Sizes of the groove regions measured by Caver. Caver uses beads with various sizes to probe the dimension of any water permeable cavity, such as the groove region of cyt bo_3 here. The maximum radius found among used beads along the groove region for the wild type and that for ΔTM0 are shown here as a metric for the size of the respective groove regions. (*D*) Separation of the headgroup of UQ8 from cyt bo_3. The separation was being measured from the center of mass of TM1. Vertical separations parallel to the membrane normal was discarded. (*E*) Distributions for RMSD of the headgroup of UQ8. (*F*) Molecular visualizations for the positions of the headgroup of UQ8. Here, snapshots along MD simulations are overlaid on one another with the coloring follows the color bar below. For clarity, only the benzene ring of UQ8 is shown.

contrast, a clear movement of the UQ8 headgroup away from cyt *bo*$_3$ is observed for ΔTM0. TM0 impedes the exit of UQ8 from cyt *bo*$_3$ and hence could serve to stabilize the binding of the reduced ubiquinol-8 substrate to cyt *bo*$_3$. Furthermore, the molecular simulations show that TM0 is flexible and can tilt with different angles with respect to the membrane normal (*SI Appendix*, Fig. S11 *C* and *D*). Thus, it is possible that, upon conformational changes of TM0, the oxidized UQ8 product of the reaction can leave cyt *bo*$_3$ within the timeframe of around 5 ms for each catalytic turnover of cyt *bo*$_3$ with ubiquinol-8.

Discussion

The cyt *bo*$_3$ ubiquinol-8 oxidase from *E. coli* is a member of the A family of proton-pumping heme–copper oxygen reductases. Most enzymes in this large family of enzymes utilize reduced cyt *c* to provide electrons required to reduce O_2 to H_2O. However, cyt *bo*$_3$ uses membrane-bound quinol as an electron source and cannot use cyt *c*. The A-family quinol oxidases, including cyt *bo*$_3$, evolved from the much larger group of cyt *c* oxidases. The quinol oxidases have “lost” the cyt *c* docking site on subunit II as well as the redox-active Cu_A in subunit II that shuttles electrons from cyt *c* to the enzyme active site where O_2 is reduced. The quinol oxidases have also gained the ability to directly oxidize reduced quinol within the membrane bilayer. Cyt *bo*$_3$, for example, can oxidize at least 200 ubiquinol-8 per second.

For many years it was thought that cyt *bo*$_3$ contained two separate quinone binding sites, a high-affinity and low-affinity site. However, recent biochemical studies indicate only one site (10), a conclusion fully consistent with the structural data presented in the current work. Previous work has demonstrated the following.

1. Interactions between cyt *bo*$_3$ and bound UQ8 stabilize the one-electron–reduced ubisemiquinone state of UQ8. The unpaired electron in the semiquinone has been used to probe hydrogen bonding between the ubisemiquinone and the surrounding protein.
2. Mutations of R71^{I}, D75^{I}, H98^{I}, and Q101^{I} can eliminate enzyme activity and alter or eliminate the stabilization of the semiquinone (9, 10, 12, 13). Spectroscopic studies (14–16) indicate that the O1 carbonyl of the ubisemiquinone is hydrogen bonded to the sidechain of D75^{I} and to N_ε of R71^{I} and that the O4 carbonyl is hydrogen bonded to N_ε of H98^{I}. The interaction of Q101^{I} with the ubisemiquinone is much weaker, suggesting proximity but not direct hydrogen bonding (15). The hydrogen bonds between the O1 carbonyl to D75^{I} and N_ε of R71^{I} are both out of the plane of the quinone ring and are on opposite sides of the ring (14). The hydrogen bond between D75^{I} and the O1 carbonyl is close to perpendicular to the plane of the UQ8 ring.
3. Whereas mutations of R71^{I}, D75^{I}, and H98^{I} can eliminate or reduce catalytic function and eliminate or alter the EPR signal from the ubisemiquinone state, these mutations do not result in dissociation of the bound UQ8 (10).
4. The quinone-analog inhibitor HQNO binds stoichiometrically to cyt *bo*$_3$ at the same site as the headgroup of UQ8 and eliminates both catalytic activity and stabilization of the ubisemiquinone radical but does not displace the bound quinone (9).

The current structures provide explanations for the biochemical and spectroscopic observations.

1. Both of the cryo-EM structures show a single UQ8 bound to cyt *bo*$_3$. This is also the case for the structure recently reported by Su et al. (20). There is no indication of the existence of a second binding site for UQ8 as previously proposed (9, 11).
2. In both structures (Table 1), carbonyl O1 of the UQ8 headgroup is close to the carboxyl of D75^{I} as well as the guanidinium sidechain of R71^{I} (both N_ε and N_η), consistent with the hydrogen bonds between D75^{I} and R71^{I} (N_ε) to the bound ubisemiquinone carbonyl O1 indicated by spectroscopic studies. The hydrogen bonds to carbonyl O1 are out of the plane of the quinone ring and are on opposite sides of the ring. As predicted by ENDOR spectroscopy, the hydrogen bond between D75 and carbonyl O1 is nearly perpendicular to the quinone ring, which is consistent with the structure from the MSP-nanodisc preparation (14).
3. In both the cryo-EM structures, UQ8 is fully oxidized, and the metal centers of the enzyme are also oxidized. The anionic ubisemiquinone could and likely does interact differently with the surrounding protein residues than either the fully oxidized or fully reduced UQ8. The current work indicates, however, that the structural changes that occur upon changing the redox state of the quinone and/or protein are relatively small and do not involve major changes in quinone location.
4. The hydrophobic isoprene sidechain of bound UQ8 is clamped to the protein by TM0 on one side and TM1 and TM3 on the other side. As a result, mutations that eliminate the hydrogen bonds between the protein and carbonyls O1 and O4 of the UQ8 headgroup do not cause the dissociation of UQ8 from the protein although function is eliminated (10).
5. The TM0 clamp on the hydrophobic tail of UQ8 also explains how inhibitors such as HQNO can displace the headgroup of UQ8 while the UQ8 remains bound to the protein (9). The recently reported structure of the cyt *bo*$_3$ homolog *B. subtilis* cyt *aa*$_3$-600 bound to iodo-HQNO shows that this small molecule inhibitor forms hydrogen bonds to the same residues that hydrogen bond to the quinone headgroup (19). The TM0 clamp holds the hydrophobic tail of UQ8 to the protein, preventing dissociation under the conditions of these experiments. This clamp-like function of TM0 is supported by computational studies.
6. The turnover of cyt *bo*$_3$ with ubiquinol-8 requires that the reduced substrate must bind to the enzyme, get oxidized, and dissociate as the oxidized product at least once every 5 ms. From the structures reported here, it seems likely that the substrate/product exchange would be facilitated by protein dynamics to open and close the protein clamp formed by TM1, TM3, and most critically TM0. Although not definitive, the data from alternate cryo-EM maps suggest multiple conformations of this region of the protein, consistent with this proposal. This suggestion is supported by MD studies that show conformational flexibility of TM0 in particular.
7. A Zn^{2+} binding site consisting of four methionines, M273^{I}, M186^{II}, M189^{II}, and M106^{IV}, is located at the periplasmic surface of the protein. M273^{I}, M186^{II}, and M189^{II} are conserved in the cyt *aa*$_3$-600 menaquinol oxidase from *B. subtilis*, but none of the methionines are conserved in cyt *c* oxidases. Zn^{2+} has been shown to inhibit cyt *c* oxidases as well as cyt *bo*$_3$ (30, 31). At low concentrations, Zn^{2+} is thought to inhibit enzyme reduction by quinol or the coupled release of protons (from quinol oxidation) but not affect proton uptake (32, 33). The structure suggests that the Zn^{2+} may block the proton-exiting pathway in cyt *bo*$_3$.
8. Two intriguing findings in the current work are 1) the different conformational states of H98^{I} and 2) the likely hydrogen bond between E14^{I} and H98^{I} when H98^{I} is flipped away from the bound quinone. E14^{I} and H98^{I} are located at the periplasmic ends of TM0 and TM2, respectively, and a hydrogen bond between them might serve to tether the TM0 clamp to the rest of the protein, locking in the bound quinone.

We would like to speculate, however, that the mobile H98^{I} along with E14^{I} may assist in the transfer of the protons from ubiquinol-8 to the periplasmic bulk solution upon oxidation of the quinol. H98^{I} in conformation 1 is in position to take a proton from the HO-4 hydroxyl of ubiquinol-8. In conformation 2, the protonated imidazole of H98^{I} could transfer its proton to the carboxyl of E14^{I} as part of a shuttle mechanism to facilitate the release of protons to the bulk solution.

A previous fourier transform infrared spectroscopy study demonstrated that $D75^{I}$ becomes protonated upon full reduction of the cyt *bo*$_3$ (17), consistent with proton transfer to $D75^{I}$ from reduced ubiquinol-8 upon binding of the substrate to the protein. According to this scenario, one-electron oxidation of anionic ubiquinol-8 would be accompanied by transfer of the second proton from ubiquinol-8 to $H98^{I}$, forming the anionic semiquinone which is stabilized by the cationic $R71^{I}$. As a result, formation of the anionic ubisemiquinone upon the one-electron oxidation of ubiquinol-8 results in the protonation of both $D75^{I}$ and $H98^{I}$. Transfer of the second electron from the bound quinol forms the fully oxidized UQ8 product, which then dissociates from the protein. The protons bound to both $D75^{I}$ and $H98^{I}$ must be released to the solution before the next round of quinol oxidation is initiated. This sequence of electron and proton transfer is summarized below and also in *SI Appendix*, Fig. S10.

ubiquinol binding

1. $D75^{I}\text{-COO}^{-} + UQH_2 \rightleftarrows D75^{I}\text{-COOH} + UQH^{-}$

first electron transfer and formation of ubisemiquinone

2. $Fe^{3+}_{\text{heme b}} + D75^{I}\text{-COOH} + H98^{I}\text{-N}_{\varepsilon} + UQH^{-} \rightleftarrows Fe^{2+}_{\text{heme b}}$
$+ D75^{I}\text{-COOH} + H98^{I}\text{-N}_{\varepsilon}H^{+} + UQ^{-\bullet}$

second electron transfer

3. $Fe^{3+}_{\text{heme b}} + UQ^{-\bullet} \rightleftarrows Fe^{2+}_{\text{heme b}} + UQ$

proton shuttle

4. $H98^{I}\text{-N}_{\varepsilon}H^{+} + E14^{I}\text{-COO}^{-} \rightleftarrows H98^{I}\text{-N}_{\varepsilon} + E14^{I}\text{-COOH}$
5. $E14^{I}\text{-COOH} + H_2O(\text{bulk water}) \rightleftarrows E14^{I}\text{-COO}^{-}$
$+ H_3O^{+}(\text{bulk water})$

proton transfer

6. $D75^{I}\text{-COOH} + H98^{I}\text{-N}_{\varepsilon} \rightleftarrows D75^{I}\text{-COO}^{-} + H98^{I}\text{-N}_{\varepsilon}H^{+}$
7. repeat steps 4 and 5

The flipping of $H98^{I}$ and proton transfer to $E14^{I}$ and subsequently to bulk solution is suggested as a proton shuttle mechanism to facilitate release of protons to the periplasmic bulk aqueous phase. Transfer of the proton from $D75^{I}$ to $H98^{I}$ for subsequent transfer to the bulk solution (via $E14^{I}$) would require water to enter between $D75^{I}$ and $H98^{I}$ to complete the pathway for proton transfer. Computational studies show that water from the bulk solution can access the region of the protein around the quinone headgroup, which is essential for proton transfer to the bulk accompanying oxidation of the quinol. TM0 prevents phospholipids from blocking the access of water to this region and effectively helps form a water channel between the bulk and the quinol headgroup. Both $D75^{I}$ and $H98^{I}$ are located on the same side of the ubiquinone ring, so a water-mediated pathway from proton diffusion between these residues appears reasonable. The role of dynamics at the quinone site, both for substrate binding/product dissociation as well as for proton transfer will require further experimental and computational work to clarify.

Finally, a few remarks are justified in comparing structures of the same membrane protein using two different biochemical approaches. The SMA copolymer avoids the use of traditional detergents and results in a nanodisc containing the protein and associated endogenous lipids. The MSP nanodisc–reconstituted protein is first isolated using a traditional detergent. The choice of detergent determines the extent of removal of endogenous lipids. The purified protein is then reconstituted using exogenous phospholipids in nanodiscs stabilized by the MSP protein. Both approaches yielded structures with resolution of at least 2.55 Å. The protein structures are essentially the same using the two approaches.

It is also noteworthy that both structures contain numerous bound phospholipids. The five PE molecules resolved in the SMA-purified cyt *bo*$_3$ have corresponding bound phospholipids in the structure of the MSP nanodisc–reconstituted protein.

Materials and Methods

Part I: For the SMA-Purified cyt *bo*$_3$.

Bacterial strain and growth conditions. Cyt *bo*$_3$ is abundant in *E. coli* and naturally has an affinity to Ni-NTA (nickel-nitrilotriacetic acid) resin. The enzyme was expressed natively in the *E. coli* strain C43 (DE3). The cells were grown in Luria broth medium at 25 °C under high aerobic conditions (2-L cultures in 6-L flasks). Cells grown overnight and were harvested by centrifugation at 5,000 × *g* for 10 min at 4 °C.

Membrane preparation and protein purification. Harvested cells were resuspended in a buffer containing 50 mM KH_2PO_4 pH 8.0, 1 mM EDTA (ethylenediaminetetraacetic acid), and 1% protease inhibitor mixture (Sigma). This suspension was passed five times through a microfluidizer at a pressure of 15,000 psi to disrupt the cells. The cell extract was centrifuged at 48,000 × *g* for 20 min to remove cell debris. Membranes were obtained after centrifugation at 180,000 × *g* for 4 h and stored at −80 °C. On the day of purification, the membrane pellet was solubilized using the SMA copolymer SMA 3000HNA (styrene maleic acid copolymer ca. 3:1 molar ratio of styrene:maleic acid) kindly provided by Cray Valley USA LLC (now Total Petrochemicals & Refining USA, Inc.). The SMA solution was added drop wise to a final concentration of 1.0% (wt/vol) with gentle stirring. After incubation for 2 h at room temperature, the solution was centrifuged at 180,000 × *g* for 20 min to remove insoluble material. The supernatant was mixed with 2 mL Nuvia IMAC Ni-Charged Resin (Bio-Rad) and incubated overnight at 4 °C with gentle agitation. Following packing through a column, the resin was washed twice with 30 mL buffer containing 50 mM Tris-HCl pH 8.0, 500 mM NaCl to remove loosely bound protein. After elution with 50 mM Tris-HCl pH 8.0, 300 mM NaCl, and 200 mM imidazole, the peak fractions were pooled, concentrated, and loaded onto an ENrich SEC 650 10 × 300 Column (Bio-Rad) equilibrated with a buffer containing 20 mM Tris-HCl pH 7.5, 50 mM NaCl. The purest and the most-concentrated fractions of cyt *bo*$_3$ were concentrated to 7.5 mg/mL using a Millipore 100-kDa cutoff concentrator and used immediately for cryo-EM grid preparation.

Cryo-EM grid preparation and data collection. Purified samples (3 μL) were applied to a freshly glow-discharged 300 mesh Quantifoil R 2/1 gold grid and blotted for 2.5 to 4 s using a blotting force of −5 at 8 °C and 100% humidity in a FEI Vitrobot Mark IV (Thermo Fisher). Grids were plunge frozen in liquid ethane and stored in liquid nitrogen. Data were collected at the West Campus Cryo-EM Core at Yale University on a 300 keV FEI Titan Krios microscope. A Gatan K3 summit camera with energy filter was used in counting mode, and 9,060 micrograph images were collected. Data collection was performed using a dose of 65 $e^{-}/Å^{2}$ across 50 frames (60 ms per frame) at a dose rate of 15.1 e^{-}/pix/s using a set defocus range of −1.2 to −2.0 μm. A 100-μm objective aperture was used. Automated data collection was performed using SerialEM (34).

Data processing. Beam-induced movement of each micrograph was corrected using MotionCor2 (35), and contrast transfer function (CTF) estimation was calculated using Gctf (36). Initial 71,627 particles were picked from 1,000 micrographs using autopicking and generated initial two-dimensional (2D) class averages by RELION (37) as the templates for automatic particle picking of the entire dataset by Gautomatch (https://www.mrc-lmb.cam.ac.uk/kzhang/). Finally, 2,961,445 particles were picked from 9,060 micrographs. Subsequent data processing was carried out in cryoSPARC (38). An initial map of cyt *bo*$_3$ was obtained by ab initio 3D classification and used as a reference for the multirefine procedure in cryoSPARC (38), producing intermediate maps of the cyt *bo*$_3$ structures. A total of 562,676 particles were used to refine the cyt *bo*$_3$ to 2.56-Å resolution. Subsequently, two classes of particles were separated from the 562,676 particles to construct maps to better resolve water molecules in the proton conducting channel (Map 1) and bound lipids (Map 2) at 2.55- and 2.64-Å resolution, respectively. To study different states of the UQ8, the separation of 562,676 particles was done again by focused classification on the UQ8 region. Another round of 3D classification without an alignment was used to generate four maps of different states of bound UQ8 (Map 3 to 6), as shown in *SI Appendix*, Fig. S1.

Model building, refinement, and validation. First, the 3.5-Å crystal structure of cyt *bo*$_3$ from *E. coli* (1FFT.pdb) (12) was fitted into the map using University of California, San Francisco Chimera version 1.13.1 (39), then side chains of the model were manually adjusted using Coot according to the map. UQ8, lipids, and waters were added manually and the model was refined with *phenix.real_space_refine* (15) with geometric constraints.

Figures were generated using UCSF ChimeraX (40) and Pymol (The PyMOL Molecular Graphics System, Schrödinger, LLC).

Part II: For cyt *bo*$_3$ Prepared in MSP Nanodiscs.

Protein purification. *E. coli* BL21 Star (DE3) strain was grown at 20 °C in 2xYT media after induction with 1 mM isopropylthio-β-galactoside. Bacteria were collected and resuspended in 20 mM Hepes pH 7.5, 150 mM NaCl, and a tablet of complete (EDTA-free) protease inhibitor (Roche). Cells were disrupted by sonication, followed by a 20-min centrifugation at 18,000 × *g*. The pellet was resuspended and incubated in cold 0.1 M Na_2CO_3 pH 11.0 for 30 min on ice, followed by a 30-min centrifugation at 100,000 × *g*. The membrane pellet was solubilized in 20 mM Hepes pH 7.5, 150 mM NaCl, 20 mM imidazole, and 1% (wt/vol) DDM for 1 h at 4 °C. Insoluble material was removed by centrifugation at 100,000 × *g* for 30 min. The solubilized fraction was loaded onto a Ni-NTA column (Qiagen) preequilibrated with 20 mM Hepes pH 7.5, 150 mM NaCl, and 0.02% DDM. Proteins were eluted with 150 mM imidazole in the same buffer.

The eluted proteins were incorporated into lipid nanodiscs with a 1:250:5 molar ratio of protein: POPG: membrane scaffold protein 1D1 (MSP1D1) and 1 mM $ZnCl_2$. This mixture was incubated at 4 °C for 2 h with gentle agitation. Reconstitution was initiated by removing detergent by incubating with Bio-beads (Bio-Rad) at 4 °C overnight with constant rotation. Bio-beads were removed, and the nanodisc reconstitution mixture was bound again to Ni-NTA resin at 4 °C for 2 h to remove free nanodiscs. The protein was eluted with 150 mM imidazole. The eluted protein was further purified by loading on a Superdex 200 Increase 10/300 GL size-exclusion column (GE Healthcare Life Sciences) in gel filtration buffer (20 mM Hepes pH 7.0 and 150 mM NaCl).

Purified protein nanodiscs were concentrated to 2.6 mg/mL using a 100-kDa concentrator (Amicon). A total of 3 μL of sample was added to a glow discharged (PELCO easiGlow) 0.6/1-μm holey gold grid (Quantifoil UltrAuFoil) and blotted for 4 s using the Vitrobot system (Thermo Fisher) before plunging immediately into liquid ethane for vitrification. The plunger was operating at 4 °C with 100% humidity. Images were collected on a Titan Krios electron microscope (FEI) equipped with a K3 direct electron detector (Gatan) operating at 0.832 Å per pixel in counting mode using the Leginon software package. Data collection was performed using a dose of 58 $e^-/Å^2$ across 50 frames (50 ms per frame) at a dose rate of 16 e^-/pix/s, using a set defocus range of −0.5 to −1.5 μm. A 100-μm objective aperture was used. A total of 3,446 micrographs were collected.

Data processing. Movie frames of 3,446 micrographs were aligned using the MotionCor2 algorithm as implemented in RELION3 (41). The motion-corrected averages were denoised using JANNI, then particles were picked from the denoised micrographs using CrYOLO. The resulting coordinates were imported into cryoSPARC version 3.1 along with the motion corrected averages. CTF estimation was performed using Patch CTF as implemented in CryoSPARC version 3.1 (38) on RELION motion-corrected averages.

The initial set of 544,868 particle coordinates were imported into cryoSPARC for extraction, 2D classification, ab initio reconstruction, and heterogeneous refinement, which resulted in 195,000 particles. Subsequent homogeneous refinement of the selected particles resulted a map at 2.72 Å. Bayesian polishing of this particle set in RELION 3.1 (37) followed by refinement using CryoSPARC resulted in a 2.52-Å reconstruction. The same set of particles was subjected to a second round of Bayesian polishing, import of this class into cryoSPARC, followed by nonuniform refinement including per particle defocus refinement and refinement of higher-order CTF parameters, gave a map at 2.26-Å reconstruction. Hetero refinement with five identical models resulted in one major high-resolution class with 110,000 particles. The subset of 95,000 particles from a second round of hetero refinement with only two classes (one filtered at 20 Å) was used for nonuniform refinement. Nonuniform refinement including per particle defocus refinement and refinement of higher-order CTF parameters gave the final map, a 2.19-Å reconstruction. This is shown in *SI Appendix*, Fig. S2. An atomic model of the protein was built in Coot (42) starting from a cyt *bo*$_3$ model (Protein Data Bank code: 1FFT) as a starting model. Model and density visualizations were prepared using UCSF Chimera (39) and ChimeraX (40).

Part III: Computational Studies.

MD simulations. Two models, the wild-type cyt *bo*$_3$ and the cyt *bo*$_3$ with TM0 removed (ΔTM0), were constructed for MD simulations. The wild-type cyt *bo*$_3$ was based on the structure determined with MSP nanodiscs reported in this work.

The mutant, ΔTM0, was constructed from the wild type by removing residues 1 to 38 of subunit I of the protein. These residues correspond to TM0 and its related coil exposed to the bulk solution.

Each of these two models was uploaded to the Orientations of Proteins in Membranes database (43) to determine the protein alignment in a lipid bilayer, followed by embedding each aligned model in a lipid bilayer using the Membrane Builder tool of CHARMM-GUI (44–47). In this study, a simplified lipid composition with 75% 1-Palmitoyl-2-Oleoyl-sn-Glycero-3-Phosphoethanolamin and 25% POPG was employed to mimic a bacterial lipid bilayer (48). After embedding our cyt *bo*$_3$ models into lipid bilayers, oxidized UQ8 were put back to the UQ8 binding pocket resolved in this study through structural alignment in VMD (Visual Molecular Dynamics Program) (49). The resulting membrane systems were solvated with counter ions and with an ion concentration of 0.15 M. Each of these systems was then relaxed by MD for 50 ns with the backbone of cyt *bo*$_3$ and heavy atoms of UQ8 constrained, followed by an unconstrained MD simulation of 500 ns using NAMD 2.14 (50) at 300 K. All parameters used in our MD simulations were adopted from the CHARMM36m force field (51).

Contact measurement. Along the trajectory produced from each MD simulation, a contact between UQ8 and cyt *bo*$_3$ was identified whenever a heavy atom of UQ8 came within 4 Å of a heavy atom of cyt *bo*$_3$. A heavy atom of UQ8 can simultaneously make contacts with multiple heavy atoms of cyt v provided they are close enough to one another. For the wild-type cyt *bo*$_3$, such measurement was performed with respect to the non-TM0 part of cyt *bo*$_3$ as well as for TM0. Results for these two parts add up to be the total number of contacts UQ8 made with cyt *bo*$_3$. For ΔTM0, only the non-TM0 part of cyt *bo*$_3$ was considered.

Data Availability. Protein structure coordinates and maps data have been deposited in Protein Data Bank https://www.rcsb.org/ (7CUB, 7CUW, 7CUQ, and 7N9Z) and Electron Microscopy Databank https://www.ebi.ac.uk/emdb/ (EMD-30471, EMD-30475, EMD-30474, EMD-30817, EMD-30819, EMD-30818, and EMD-24265). The data will be accessible upon publication. All other study data are included in the article and/or *SI Appendix*.

ACKNOWLEDGMENTS. We thank Dr. Shenping Wu at the Yale West Campus Advanced Biosciences Center for assistance with the SMA nanodisc data collection. Data for the MSP nanodisc structure was collected at the Columbia University Cryo-Electron Microscopy Center. This work was supported by National Key Research and Development Program of China 2020YFA0509400 (to J.P.); the Priority Academic Program Development of Jiangsu Higher Education Institutions (Integration of Chinese and Western Medicine); the Natural Science Foundation of Jiangsu Province for Young Scientists BK20190806 (to B.L.); Chemical Sciences, Geosciences and Biosciences Division, Office of Basic Energy Sciences, Office of Sciences, US Department of Energy Grant No. DE-FG02-87ER13716 (to R.G.); startup funds from Yale University (to K.Z.); and Rudolf J. Anderson Fellowship awards (to L.H.). Cryo-EM data on cyt *bo*$_3$ in MSP nanodiscs was collected at the Columbia University Cryo-Electron Microscopy Center with assistance of Bob Grassucci and Zhening Zhang. Computational studies reported in this work were supported by NIH under Award No. P41GM104601. We also acknowledge the Texas Advanced Computing Center at The University of Texas at Austin for providing HPC (high-performance computing) resources that have contributed to the research results reported within this paper.

1. M. M. Pereira, M. Santana, M. Teixeira, A novel scenario for the evolution of haem-copper oxygen reductases. *Biochim. Biophys. Acta* **1505**, 185–208 (2001).
2. R. K. Poole, Bacterial cytochrome oxidases. A structurally and functionally diverse group of electron-transfer proteins. *Biochim. Biophys. Acta* **726**, 205–243 (1983).
3. K. Matsushita, L. Patel, H. R. Kaback, Cytochrome o type oxidase from *Escherichia coli*. Characterization of the enzyme and mechanism of electrochemical proton gradient generation. *Biochemistry* **23**, 4703–4714 (1984).
4. Y. Anraku, R. B. Gennis, The aerobic respiratory chain of *Escherichia coli*. *Trends Biochem. Sci.* **12**, 262–266 (1987).
5. M. Saraste *et al*., Cytochrome o from *Escherichia coli* is structurally related to cytochrome aa3. *Ann. N. Y. Acad. Sci.* **550**, 314–324 (1988).
6. P. Brzezinski, R. B. Gennis, Cytochrome c oxidase: Exciting progress and remaining mysteries. *J. Bioenerg. Biomembr.* **40**, 521–531 (2008).
7. A. Puustinen, M. Finel, M. Virkki, M. Wikström, Cytochrome o (bo) is a proton pump in *Paracoccus denitrificans* and *Escherichia coli*. *FEBS Lett.* **249**, 163–167 (1989).
8. A. Puustinen, M. Finel, T. Haltia, R. B. Gennis, M. Wikström, Properties of the two terminal oxidases of *Escherichia coli*. *Biochemistry* **30**, 3936–3942 (1991).
9. L. L. Yap *et al*., The quinone-binding sites of the cytochrome bo3 ubiquinol oxidase from *Escherichia coli*. *Biochim. Biophys. Acta* **1797**, 1924–1932 (2010).
10. S. K. Choi *et al*., Location of the substrate binding site of the cytochrome bo_3 ubiquinol oxidase from *Escherichia coli*. *J. Am. Chem. Soc.* **139**, 8346–8354 (2017).
11. S. K. Choi, M. T. Lin, H. Ouyang, R. B. Gennis, Searching for the low affinity ubiquinone binding site in cytochrome bo_3 from *Escherichia coli*. *Biochim. Biophys. Acta Bioenerg.* **1858**, 366–370 (2017).
12. J. Abramson *et al*., The structure of the ubiquinol oxidase from *Escherichia coli* and its ubiquinone binding site. *Nat. Struct. Biol.* **7**, 910–917 (2000).
13. P. Hellwig, T. Yano, T. Ohnishi, R. B. Gennis, Identification of the residues involved in stabilization of the semiquinone radical in the high-affinity ubiquinone binding site in cytochrome bo(3) from *Escherichia coli* by site-directed mutagenesis and EPR spectroscopy. *Biochemistry* **41**, 10675–10679 (2002).

14. C. Sun *et al*., Q-band electron-nuclear double resonance reveals out-of-plane hydrogen bonds stabilize an anionic ubisemiquinone in cytochrome bo$_3$ from *Escherichia coli*. *Biochemistry* **55**, 5714–5725 (2016).
15. M. T. Lin *et al*., Interactions of intermediate semiquinone with surrounding protein residues at the Q(H) site of wild-type and D75H mutant cytochrome bo3 from *Escherichia coli*. *Biochemistry* **51**, 3827–3838 (2012).
16. M. T. Lin, R. I. Samoilova, R. B. Gennis, S. A. Dikanov, Identification of the nitrogen donor hydrogen bonded with the semiquinone at the Q(H) site of the cytochrome bo3 from *Escherichia coli*. *J. Am. Chem. Soc.* **130**, 15768–15769 (2008).
17. P. Hellwig, B. Barquera, R. B. Gennis, Direct evidence for the protonation of aspartate-75, proposed to be at a quinol binding site, upon reduction of cytochrome bo3 from *Escherichia coli*. *Biochemistry* **40**, 1077–1082 (2001).
18. Z. Ding, C. Sun, S. M. Yi, R. B. Gennis, S. A. Dikanov, The ubiquinol binding site of cytochrome *bo*$_3$ from *Escherichia coli* accommodates menaquinone and stabilizes a functional menasemiquinone. *Biochemistry* **58**, 4559–4569 (2019).
19. J. Xu *et al*., Structure of the cytochrome *aa* $_3$ -600 heme-copper menaquinol oxidase bound to inhibitor HQNO shows TM0 is part of the quinol binding site. *Proc. Natl. Acad. Sci. U.S.A.* **117**, 872–876 (2020).
20. C. C. Su *et al*., A 'Build and Retrieve' methodology to simultaneously solve cryo-EM structures of membrane proteins. *Nat. Methods* **18**, 69–75 (2021).
21. C. Sun, R. B. Gennis, Single-particle cryo-EM studies of transmembrane proteins in SMA copolymer nanodiscs. *Chem. Phys. Lipids* **221**, 114–119 (2019).
22. S. C. Lee *et al*., A method for detergent-free isolation of membrane proteins in their local lipid environment. *Nat. Protoc.* **11**, 1149–1162 (2016).
23. S. C. Lee, N. L. Pollock, Membrane proteins: Is the future disc shaped? *Biochem. Soc. Trans.* **44**, 1011–1018 (2016).
24. A. J. Rothnie, Detergent-free membrane protein purification. *Methods Mol. Biol.* **1432**, 261–267 (2016).
25. J. M. Dörr *et al*., The styrene-maleic acid copolymer: A versatile tool in membrane research. *Eur. Biophys. J.* **45**, 3–21 (2016).
26. I. G. Denisov, S. G. Sligar, Nanodiscs in membrane biochemistry and biophysics. *Chem. Rev.* **117**, 4669–4713 (2017).
27. S. G. Sligar, I. G. Denisov, Nanodiscs: A toolkit for membrane protein science. *Protein Sci.* **30**, 297–315 (2021).
28. I. G. Denisov, S. G. Sligar, Nanodiscs for structural and functional studies of membrane proteins. *Nat. Struct. Mol. Biol.* **23**, 481–486 (2016).
29. A. Jurcik *et al*., CAVER Analyst 2.0: Analysis and visualization of channels and tunnels in protein structures and molecular dynamics trajectories. *Bioinformatics* **34**, 3586–3588 (2018).
30. K. Faxén, L. Salomonsson, P. Adelroth, P. Brzezinski, Inhibition of proton pumping by zinc ions during specific reaction steps in cytochrome c oxidase. *Biochim. Biophys. Acta* **1757**, 388–394 (2006).
31. L. Qin *et al*., Crystallographic location and mutational analysis of Zn and Cd inhibitory sites and role of lipidic carboxylates in rescuing proton path mutants in cytochrome c oxidase. *Biochemistry* **46**, 6239–6248 (2007).
32. S. A. Weiss, R. J. Bushby, S. D. Evans, L. J. Jeuken, A study of cytochrome bo3 in a tethered bilayer lipid membrane. *Biochim. Biophys. Acta* **1797**, 1917–1923 (2010).
33. S. A. Siletsky, R. B. Gennis, Time-resolved electrometric study of the F→O transition in cytochrome c oxidase. The effect of Zn^{2+} ions on the positive side of the membrane. *Biochemistry (Mosc.)* **86**, 105–122 (2021).
34. D. N. Mastronarde, Automated electron microscope tomography using robust prediction of specimen movements. *J. Struct. Biol.* **152**, 36–51 (2005).
35. S. Q. Zheng *et al*., MotionCor2: Anisotropic correction of beam-induced motion for improved cryo-electron microscopy. *Nat. Methods* **14**, 331–332 (2017).
36. K. Zhang, Gctf: Real-time CTF determination and correction. *J. Struct. Biol.* **193**, 1–12 (2016).
37. S. H. Scheres, RELION: implementation of a Bayesian approach to cryo-EM structure determination. *J. Struct. Biol.* **180**, 519–530 (2012).
38. A. Punjani, J. L. Rubinstein, D. J. Fleet, M. A. Brubaker, cryoSPARC: Algorithms for rapid unsupervised cryo-EM structure determination. *Nat. Methods* **14**, 290–296 (2017).
39. E. F. Pettersen *et al*., UCSF Chimera–A visualization system for exploratory research and analysis. *J. Comput. Chem.* **25**, 1605–1612 (2004).
40. T. D. Goddard *et al*., UCSF ChimeraX: Meeting modern challenges in visualization and analysis. *Protein Sci.* **27**, 14–25 (2018).
41. J. Zivanov *et al*., New tools for automated high-resolution cryo-EM structure determination in RELION-3. *eLife* **7**, e42166 (2018).
42. P. Emsley, B. Lohkamp, W. G. Scott, K. Cowtan, Features and development of Coot. *Acta Crystallogr. D Biol. Crystallogr.* **66**, 486–501 (2010).
43. M. A. Lomize, I. D. Pogozheva, H. Joo, H. I. Mosberg, A. L. Lomize, OPM database and PPM web server: Resources for positioning of proteins in membranes. *Nucleic Acids Res.* **40**, D370–D376 (2012).
44. S. Jo, T. Kim, W. Im, Automated builder and database of protein/membrane complexes for molecular dynamics simulations. *PLoS One* **2**, e880 (2007).
45. S. Jo, J. B. Lim, J. B. Klauda, W. Im, CHARMM-GUI Membrane Builder for mixed bilayers and its application to yeast membranes. *Biophys. J.* **97**, 50–58 (2009).
46. E. L. Wu *et al*., CHARMM-GUI Membrane Builder toward realistic biological membrane simulations. *J. Comput. Chem.* **35**, 1997–2004 (2014).
47. S. Jo, T. Kim, V. G. Iyer, W. Im, CHARMM-GUI: A web-based graphical user interface for CHARMM. *J. Comput. Chem.* **29**, 1859–1865 (2008).
48. K. Murzyn, M. Pasenkiewicz-Gierula, Construction and optimisation of a computer model for a bacterial membrane. *Acta Biochim. Pol.* **46**, 631–639 (1999).
49. W. Humphrey, A. Dalke, K. Schulten, VMD: Visual molecular dynamics. *J. Mol. Graph* **14**, 33–38 (1996).
50. J. C. Phillips *et al*., Scalable molecular dynamics on CPU and GPU architectures with NAMD. *J. Chem. Phys.* **153**, 044130 (2020).
51. J. Huang *et al*., CHARMM36m: An improved force field for folded and intrinsically disordered proteins. *Nat. Methods* **14**, 71–73 (2017).